YALE
PEABODY
MUSEUM

JOURNAL OF MARINE RESEARCH

The *Journal of Marine Research,* one of the oldest journals in American marine science, published important peer-reviewed original research on a broad array of topics in physical, biological, and chemical oceanography vital to the academic oceanographic community in the long and rich tradition of the Sears Foundation for Marine Research at Yale University.

An archive of all issues from 1937 to 2021 (Volume 1–79) are available through EliScholar, a digital platform for scholarly publishing provided by Yale University Library at https://elischolar.library.yale.edu/.

Requests for permission to clear rights for use of this content should be directed to the authors, their estates, or other representatives. The *Journal of Marine Research* has no contact information beyond the affiliations listed in the published articles. We ask that you provide attribution to the *Journal of Marine Research.*

Yale University provides access to these materials for educational and research purposes only. Copyright or other proprietary rights to content contained in this document may be held by individuals or entities other than, or in addition to, Yale University. You are solely responsible for determining the ownership of the copyright, and for obtaining permission for your intended use. Yale University makes no warranty that your distribution, reproduction, or other use of these materials will not infringe the rights of third parties.

The wave-current interaction in the coastal area

by Homayoon Komijani[1] and Jaak Monbaliu[2]

ABSTRACT

In our investigation of the effect of wind-waves on barotropic mean flow in coastal areas, we compare two methods for calculating wave-induced force. The wave field is simulated by the near-shore spectral wave model SWAN. The wave-induced force (calculated using the radiation stress gradient and dissipation methods) and the Stokes drift are integrated in the COHERENS circulation model in the depth-averaged mode. The coupled set is validated using well-known academic test cases of planar beach and single-barred beach. Finally, in a two-dimensional test case based on Belgian coastal waters we compare simulations of mean flow using the two methods of calculating wave-induced force against field data.

We show clearly that the two methods for calculation of wave-induced force yield very different results even in depth-averaged mode, depending on the angle of incident wave. Simulation of wave-induced circulation using the wave dissipation approach gives better results than using the radiation stress gradient approach. This is clearly visible for strong wave conditions in which the wind is blowing almost parallel to the shore. Under these conditions, the white-capping type of wave breaking is the dominant dissipation mechanism; in the radiation stress gradient, the dissipation signal is not visible, because the energy loss in the spectrum is compensated by wind input.

Keywords: wave modeling, hydrodynamic modeling, wave-current interaction, radiation stress gradient, Stokes drift.

1. Introduction

The interaction between the wind-induced short gravity waves (commonly referred to as "wind-waves") and the hydrodynamic system averaged over these waves (commonly referred to as "mean flow" or "current") consists of a complex set of reciprocal processes. These processes can be categorized into two groups, namely, the effects of the hydrodynamic system on the waves and the effects of waves on the hydrodynamic system (Brown and Wolf 2009).

1. Department of Civil Engineering, Hydraulics and Geotechnics Section, KU Leuven, Kasteelpark Arenberg 40/2448 3001 Leuven, Belgium; orcid: 0000-0001-7515-0220

2. Department of Civil Engineering, Hydraulics and Geotechnics Section, KU Leuven, Kasteelpark Arenberg 40/2448 3001 Leuven, Belgium; orcid: 0000-0002-6107-4201

3. Corresponding author: *e-mail: homayoon.komijani@kuleuven.be*

The first group includes alteration of wind-wave characteristics due to hydrodynamic processes. The water level as well as the mean flow velocity affect the short gravity waves through, for example, depth modulation and Doppler shifting (Bolaños, Brown, and Souza 2014). The energy dissipation of short waves happens through processes such as depth- or steepness-induced breaking and bottom drag. Both of these processes are highly dependent on the total water depth. Thus, the modulation of total water depth will affect the wave energy level. Moreover the propagation of waves depends on the velocity of the medium. Thus, in presence of a mean flow, Doppler shifting and current refraction will alter wave energy propagation (Toffoli, Cavaleri, et al. 2011; Toffoli, Waseda, et al. 2015; Waseda, Kinoshita, and Cavaleri 2015).

The second group (on which we will focus here) includes processes through which waves affect the current. The effect of wind-induced short gravity waves on the mean flow has been known since the mid-20th century. They were first described in the works of Longuet-Higgins and Stewart (1962, 1964), who calculated the wave-induced forces on the mean flow by the gradient of the radiation stress tensor. Hasselmann (1971) used an interaction tensor and a surface mass transfer to describe the effect of the wave field on the mean flow. He also showed that the work done on the long waves by the interaction stresses is almost exactly balanced by the loss of potential energy arising from the mass transfer. Dingemans, Radder, and Vriend (1987) showed that for slowly varying wave fields, the wave force on the mean flow is almost equal to the wave energy dissipation. The scientific community is engaged in ongoing debates over the different theoretical approaches and implementations proposed for wave-current coupling in the three dimensions. (For a comprehensive review, see Bennis, Ardhuin, and Dumas [2011].) However, not much has changed in the way this problem is dealt with in the depth-averaged mode. For a complete review of depth-integrated and depth-varying approaches in the wave-current interaction physics see Babanin et al. (2017) and Smith (2006).

With an interest in application in coastal areas, we have focused on the depth-averaged mode of the wave-current interaction. The Reynolds-averaged Navier-Stokes (RANS) equations for depth-averaged quasi-Eulerian velocity are implemented in the COupled Hydrodynamic-Ecological model for REgioNal Shelf seas (COHERNS), a modular circulation model (Luyten 1999). The wind-waves are simulated using the Simulating WAves Nearshore (SWAN) model (Ris, Holthuijsen, and Booij 1994). The wave-induced force and the depth-averaged Stokes drift are calculated in a separate subroutine so that they can be included in the momentum and continuity equations. Both of the formulations for calculating wave-induced force (i.e., using radiation stress gradient and dissipation function) are implemented.

In Section 2, the governing equations used are described. For convenience, all the symbols used throughout this article are listed in Appendix A along with their description and unit. The coupling frame is described in the Section 3. A brief review of each component is given together with specification of the coupling in practice.

In Section 4, the coupled model is tested for two well-known academic test cases. In Section 4a, the planar beach test case of Haas and Warner (2009) is presented, followed in Section 4b by the single-barred beach test case of Uchiyama, McWilliams, and Restrepo (2009). The results from the coupled COHERENS-SWAN model are compared with the results reported in the literature.

An application of the coupled system in the Belgian coastal area is described in Section 5. Puzzled by the Belgian coast, with its multiple sand bars, and inspired by the planar beach test of Haas and Warner (2009) and the single-barred beach test of Uchiyama, McWilliams, and Restrepo (2009), we ran a semi-realistic one-dimensional test, presented in Section 5a, to observe how multiple bars affect the wave-induced current.

In Section 5b, we examine the effectiveness of including the wave-current interaction in hindcasting simulations. In this test, the wave-current simulation in Belgian coastal waters is carried out taking into account the interaction effects. We also compare the response of the hydrodynamic model to the wave forcing calculated once using radiation stress theory and once using the dissipation function. We do this comparison for two distinct storms. By this comparison we show clearly that the two methods give very different results even in depth-averaged mode.

Finally, in Section 6, we deliver some concluding remarks and discuss next steps for the continuation of this study.

2. Governing equations

a. Hydrodynamic model

Bennis, Ardhuin, and Dumas (2011) give the quasi-Eulerian glm2 equations in the flux format in the σ-coordinates for the momentum balance, continuity, and passive tracers. Averaging over the water column yields the depth-averaged mode of those equations. For the momentum balance in the *x*- and *y*-direction, respectively,

$$\frac{\partial(D\bar{\hat{u}})}{\partial t} + \frac{\partial[D(\bar{\hat{u}} + \bar{U}_s)\bar{\hat{u}}]}{\partial x} + \frac{\partial[D(\bar{\hat{v}} + \bar{V}_s)\bar{\hat{u}}]}{\partial y} - Df\bar{\hat{v}} + \frac{D}{\rho_0}\left(\frac{\partial p^H}{\partial x}\right) \tag{1}$$

$$= \bar{V}_s D\left(f + \frac{\partial\bar{\hat{v}}}{\partial x}\right) + \bar{U}_s D\left(\frac{\partial\bar{\hat{u}}}{\partial x}\right) + F_x^w,$$

$$\frac{\partial(D\bar{\hat{v}})}{\partial t} + \frac{\partial[D(\bar{\hat{u}} + \bar{U}_s)\bar{\hat{v}}]}{\partial x} + \frac{\partial[D(\bar{\hat{v}} + \bar{V}_s)\bar{\hat{v}}]}{\partial y} + Df\bar{\hat{u}} + \frac{D}{\rho_0}\left(\frac{\partial p^H}{\partial y}\right) \tag{2}$$

$$= \bar{V}_s D\left(\frac{\partial\bar{\hat{v}}}{\partial y}\right) - \bar{U}_s D\left(f - \frac{\partial\bar{\hat{u}}}{\partial y}\right) + F_y^w.$$

In equations 1 and 2, (x, y, z) is the Cartesian coordinate system. The $(\hat{\ })$ indicates the wave phase-averaged value of the parameter and the $(\bar{\ })$ denotes the mean value averaged over the depth. The $D = d + \hat{\zeta}$ is the total water depth where $\hat{\zeta}$ is the local phase-averaged

free surface and d is the depth of still water. The f is the Coriolis parameter, J is the wave-induced pressure, p^H is the hydrostatic pressure, which includes the atmospheric pressure at the surface, and ρ_0 is the water density. The $\bar{\hat{u}} = (\bar{\hat{u}}, \bar{\hat{v}})$ is the depth-averaged quasi-Eulerian velocity vector, which can be expressed as

$$\bar{\hat{u}} = \bar{U} - \bar{U}_s,\tag{3}$$

where $\bar{U}_s = (\bar{U}_s, \bar{V}_s)$ is the near surface two-dimensional wave's Stokes drift velocity vector and $\bar{U} = (\bar{U}, \bar{V})$ is the Lagrangian velocity vector in depth-averaged mode. The F^w is the total force induced on the mean flow over the full water column due to wind-waves.

For the continuity

$$\frac{\partial \hat{\zeta}}{\partial t} + \frac{\partial [D(\bar{\hat{u}} + \bar{U}_s)]}{\partial x} + \frac{\partial [D(\bar{\hat{v}} + \bar{V}_s)]}{\partial y} = 0.\tag{4}$$

The waves' depth-averaged Stokes drift $\bar{U}_s = (\bar{U}_s, \bar{V}_s)$ can be calculated as

$$(\bar{U}_s, \bar{V}_s) = \frac{\sigma_p E}{k_p D \tanh(k_p D)} \boldsymbol{k}_p.\tag{5}$$

In equation 5, $E_{(\sigma, \theta)}$ is the spectral density of the surface wave elevation variance, σ_p is the wave's intrinsic frequency corresponding to the peak wave energy, and k_p is the magnitude of the wave number vector corresponding to this frequency. $\boldsymbol{k}_p = (k_{px}, k_{py}) = k_p(\cos\theta, \sin\theta)$ is the wave number vector where θ is the wave's propagation direction. To prevent singularity in the breaking zone, we assume a maximum of possible individual wave height $H_{\max}$ equal to a portion of the total depth $H_{\max} = \gamma D$. The breaking coefficient γ is often considered constant or as a function of incident wave steepness or bottom slope. Here the average value of data set from Battjes and Stive (1985) is used as the constant value for breaking coefficient $\gamma = 0.73$ over the entire domain. Equation 6 for the shallow waters, is

$$\bar{U}_s = \frac{\sigma_p \boldsymbol{k}_p \gamma^2}{16 k_p^2}.\tag{6}$$

Two methods are used to calculate the depth integrated wave-induced force F^w. In the first, based on the radiation stress theory of Longuet-Higgins and Stewart (1962),

$$F_x^w = -\frac{1}{\rho_0}\left(\frac{\partial S_{xx}}{\partial x} + \frac{\partial S_{xy}}{\partial y}\right)\tag{7}$$

$$F_y^w = -\frac{1}{\rho_0}\left(\frac{\partial S_{yx}}{\partial x} + \frac{\partial S_{yy}}{\partial y}\right),$$

where the radiation stress components are given by

$$S_{xx} = \rho_0 g \int \int [n \cos^2 \theta + n - 0.5] E(f, \theta) df d\theta \qquad (8)$$

$$S_{xy} = S_{yx} = \rho_0 g \int \int [n \sin \theta \cos \theta] E(f, \theta) df d\theta$$

$$S_{yy} = \rho_0 g \int \int [n \sin^2 \theta + n - 0.5] E(f, \theta) df d\theta.$$

In equations 7 and 8, n is the ratio of wave's group velocity $c_g = \frac{\partial \sigma}{\partial k}$ to the phase velocity $c_{ph} = \frac{\sigma}{k}$.

In the second method, based on the wave dissipation terms as suggested by Ardhuin, Rascle, and Belibassakis (2007) and Bennis, Ardhuin, and Dumas (2011),

$$F_x^w = \hat{F}_{d,x} + \hat{F}_{b,x} - D\frac{\partial J}{\partial x} \qquad (9)$$

$$F_y^w = \hat{F}_{d,y} + \hat{F}_{b,y} - D\frac{\partial J}{\partial y},$$

where the force induced by wave dissipation close to the surface $\hat{\boldsymbol{F}}_d = (\hat{F}_{d,x}, \hat{F}_{d,y})$ and the force induced by wave's bottom friction $\hat{\boldsymbol{F}}_b = (\hat{F}_{b,x}, \hat{F}_{b,y})$ are,

$$\hat{\boldsymbol{F}}_d = \frac{\epsilon_{br} \boldsymbol{k}_p}{\rho_0 \sigma_p} \qquad (10)$$

$$\hat{\boldsymbol{F}}_b = \frac{\epsilon_{fr} \boldsymbol{k}_p}{\rho_0 \sigma_p}.$$

The near surface dissipation term (ϵ_{br}) and the bottom dissipation term (ϵ_{fr}) can be obtained directly from the wave model. These are the results of the dissipation modules of the wave model. The dissipation modules of the SWAN wave model calculate the dissipation as a portion of the wave action density.

The wave-induced pressure term is

$$\boldsymbol{J} = \int g \frac{k_{(\sigma)} E_{(\sigma,\theta)}}{\sinh(2k_p D)} d\sigma d\theta. \qquad (11)$$

The near surface dissipation includes the depth-induced breaking and the white-capping dissipation. In SWAN we used the formulation of Battjes and Janssen (1978) for the depth-induced wave breaking. A constant breaking coefficient $\gamma = 0.73$ is used over the entire domain. For the calculation of the white-capping dissipation in SWAN, we used the non-linear saturation-based formulation. This formulation is adapted from Alves and Banner (2003) and the wind input formulation of Yan (1987). The bottom dissipation term is calculated in SWAN using the formulation of Hasselmann et al. (1973) based on the empirical

model of the JOint North Sea WAve Project (JONSWAP) with the constant coefficient of $0.067 \text{ m}^2 \text{ s}^{-3}$. For more detail about the formulations used and their implementation, see SWAN team (2020a).

The first advantage calculating $\boldsymbol{F}^w$ using the wave dissipation terms is that it is accurate in the situations where wave dissipation due to white-capping is considerable. The second advantage of this method is that the near surface dissipation (due to the depth-induced wave breaking and/or white-capping) will be separated from the near bottom dissipation (due to bottom friction). This permits the numerical modelers to apply them respectively to the near surface layers and to the bottom boundary layer in case of three-dimensional modeling. The exact depth profile of $\boldsymbol{F}^w$ is not known. However, some shape functions are suggested in the literature to distribute this force along the water column (e.g., Uchiyama, McWilliams, and Restrepo 2009; Warner et al. 2008). On the other hand, the amount of data that needs to be transferred between wave model and hydrodynamic model is considerably lower in the first method (wave-induced force based on radiation stress gradient) when applied in coastal areas where the wave-induced force can be assumed uniform in depth.

b. Wave model

Bretherton and Garrett (1968) introduced the wave action conservation equation as

$$\frac{\partial N}{\partial t} + \nabla \cdot [(\mathbf{c_g} + \bar{\bar{\boldsymbol{u}}})N] = S. \tag{12}$$

Where $N = \frac{E}{\sigma}$ is the wave action density and is equal to the wave energy density divided by the relative frequency of the waves for an observer moving with the local current; $\mathbf{c_g}$ is the group velocity of waves and $\bar{\bar{\boldsymbol{u}}} = (\bar{\bar{u}}, \bar{\bar{v}})$ is the flow velocity of the medium or in this case the depth-averaged quasi-Eulerian velocity vector.

$S_{(\mathbf{x},\sigma,\theta,t)}$ is the sum of different sources of energy into the system and sinks of energy out of the system. It accounts for wind source of energy and three different mechanisms of wave energy dissipation. The dissipation happens through three main processes: the dissipation of energy due to bottom friction, the dissipation due to breaking of waves, and the dissipation due to white-capping. Different terms on both sides of equation 12 are highly dependent on the total water depth and mean flow of the medium where the waves are propagating. Therefore, the water level and the depth-averaged quasi-Eulerian velocity vector are transferred from the hydrodynamic model to the wave model. On the side of the wave model no new variable is added.

The list of the variables added to the hydrodynamic model is given in Table 1.

3. Coupling wave and hydrodynamic models

For the practical implementation of the coupling, two community models are used. SWAN (version 40.91) is a wave model, and COHERENS (version 2.7; Luyten et al. 2005) is a hydrodynamic model. The coupling set, designated SWAN-COHERENS, consists of these two models.

Table 1. Some of the mathematical symbols presented in the equations and the corresponding variable name in the code.

Symbol	Variables in swn_calc.f90	Variables in COHERENS
$\boldsymbol{F}_d = (F_{d,x}, F_{d,y})$	*(NSDxGL, NSDyGL)*	–
$\boldsymbol{F}_b = (F_{b,x}, F_{b,y})$	*(BSxGL, BSyGL)*	–
$\boldsymbol{U}_s = (U_s, V_s, W_s)$	*(SVxGL, SVyGL, 0)*	*(svmuatu, svmvatu, 0)*
$\boldsymbol{F}^w = (F_x^w, F_y^w)$	*(WFxGL, WFxGL)*	*(wavfatu, wavfatv)*

a. SWAN

SWAN (SWAN team, 2020b) is a well-known third-generation spectral wave model. It solves the equation of conservation of action density (Eq. 12) numerically in order to estimate wave parameters such as wave height and period. In this study we have used the SWAN version 40.72.

SWAN can run in the time-independent stationary mode or in the time-dependent non-stationary mode. The computation can be done in regular, curvilinear, or triangular mesh in the Cartesian or spherical coordinate system. The user can choose between a wide range of different formulations for sources, sinks, and numerical schemes. SWAN uses implicit numerical schemes for propagation in geographical and spectral spaces. Therefore, it is very suitable for coastal areas (SWAN team, 2020b). SWAN can run in parallel mode using message passing interface (MPI) or OpenMP libraries. The specific formulations used in SWAN for the sources and the sinks of energy are given for each test case.

b. COHERENS

COHERENS is a multipurpose three-dimensional hydrodynamic model for coastal and shelf seas (Luyten et al. 1999). COHERENS was initially developed during the years 1990 through 1998, with further developments being carried out up to 2015. It is used by about 2,000 users in more than 100 countries, which makes COHERENS an important and well-established community model (see http://odnature.naturalsciences.be/coherens/).

COHERENS solves the three-dimensional Navier-Stokes equations in flux format. It uses finite difference and discretizes the equations on an Arakawa C-grid. First, the equations are solved for water level and velocities in two-dimensional barotropic mode. Then, they are solved in three-dimensional mode for current velocity profile and vertical velocity. Finally, the equations for passive tracers, salinity, and temperature are solved. COHERENS takes account of astronomical tide by forcing water level on the boundaries calculated using the normalized tidal potential. It calculates the water level on boundaries by considering nodal amplitude and phase factors for eight components of tidal constituents. COHERENS also includes tidal forcing in the domain, but this feature is disabled in the studies reported in this study as its effect is negligible due to small domain.
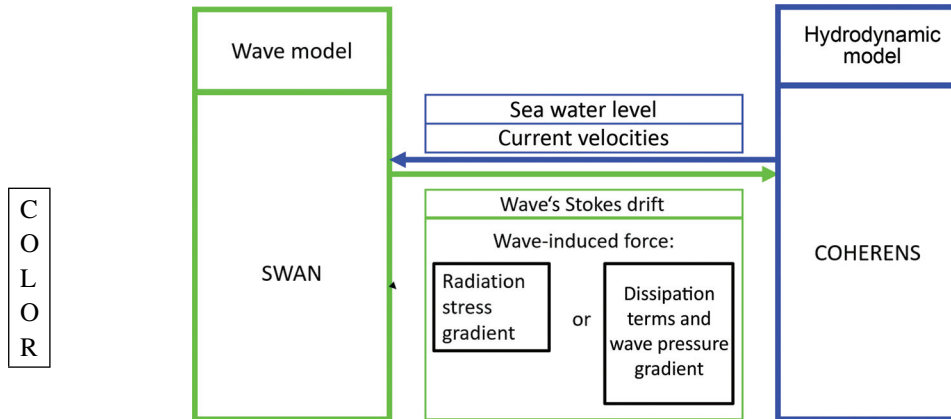
Figure 1. The coupling flowchart. The wave dependent terms wave-induced force (based on the radiation stress gradient or dissipation) and wave's Stokes drift are calculated outside the wave model and passed to the hydrodynamic model.

The current version of COHERENS can be used in a one-dimensional vertical field, in a two-dimensional horizontal field, or in a complete three-dimensional field. The grid can be defined as rectangular or curvilinear in horizontal directions and as generalized σ-coordinates in the vertical direction. The spacing in generalized σ-coordinates can be non-uniform not only in vertical direction but also in horizontal direction in compliance with the s-coordinate system (Song and Haidvogel 1994). In our study, we used COHERENS in two-dimensional depth-averaged mode. COHERENS takes advantage of parallel computation using MPI. Sub-grid nesting can be applied for two-dimensional and three-dimensional cases.

c. COHERENS-SWAN

The coupling occurs in two ways. In one, the water level and the depth-averaged velocity vector are passed from COHERENS to SWAN. In the other, wave-induced force and the depth-averaged Stokes drift velocity vector are passed from SWAN to COHERENS.

In order to calculate the wave dependent terms, an extra subroutine is added to SWAN. (The code is available from the Marine Data Archive [Komanji and Monbaliu 2018].)

The flowchart of the coupled set is presented in Figure 1. In the present study, the coupling is in depth-averaged mode only, and no coupler is used. Therefore, exchange of information is done directly by using MPI routines. Direct usage of MPI routines makes the coupling procedures transparent and keeps the size of the coupled set to a minimum, which in turn results in more efficient simulation. This approach also minimizes the costs of updating the coupled-set with new version releases of each component.

In the coupled-set, each model runs on a separate group of processors. The two models can have different time steps and spatial resolutions. The spectral wave model usually has a much longer time step than the circulation model. Since the interpolation happens over the whole domain, it does affect the performance of the coupled set drastically. Therefore it is important to keep the information exchange time step between the models independent of the time step of each model. A warm-up time is foreseen before the start of exchange of data between the components. The coupling time steps for SWAN to COHERENS exchange of information ($\Delta t\,W2H$) and for COHERENS to SWAN exchange of information ($\Delta t\,H2W$) can be different from each other and can be different from the calculation time step of each model. The only limitation is that the exchange time steps must be an integer number of time steps of each model. The interpolation of exchanged data happens internally in each model after receiving information over the full grid. Thus, the internal interpolation routines are used within each model.

On the side of the hydrodynamic model, the terms $\bar{\bar{\boldsymbol{u}}} = (\bar{\bar{u}}, \bar{\bar{v}})$ from equations 1 and 2 and $\hat{\zeta}$ from equation 4 are passed to the wave model to update the medium velocity vector and total water depth used in the wave action conservation equation (Eq. 12).

On the side of the wave model, the terms F_x^w, F_y^w from equation 7 and $\bar{U}_s$, $\bar{V}_s$ from equation 5 are calculated in a new subroutine. The user can choose to calculate the wave-induced force using either radiation stress gradient or wave dissipation.

The calculated terms are then passed to the hydrodynamic model. They are added in COHERENS, respectively, to equations 1, 2, and 4.

The central difference method is used to calculate the wave dependent terms of wave pressure gradient and radiation stress gradient (see Eq. 7 and 9). The forward difference method is used for the calculation of the Stokes drift gradients in the hydrodynamic equations (see Eq. 1, 2, and 4).

Both of the models used in this coupling practice have open source codes, available with steering files and input files necessary to set up each test case, from the Marine Data Archive (Komijani and Monbaliu 2018). The interested reader will find a short manual explaining the structure of this data.

4. Academic test cases

a. Planar beach

The planar beach is a simple test to illustrate wave-induced alongshore and cross-shore velocities and set-up. The domain is rectangular: 1,200-m long cross-shore (x-direction, positive eastward), 200-m wide alongshore (y-direction, positive northward). The bottom topography starts with 12-m depth offshore at x $=$ 0 m and with a slope of 1:80 that meets the free sea surface at x $=$ 960 m. The grid spacing is 20 m in both x- and y-directions. The incident wave spectrum is simulated in SWAN combining a JONSWAP shape spectrum with a directional distribution function. The JONSWAP spectrum has the peak period of 10 s and significant wave height of 2 m with 10° angle at x $=$ 0 with respect
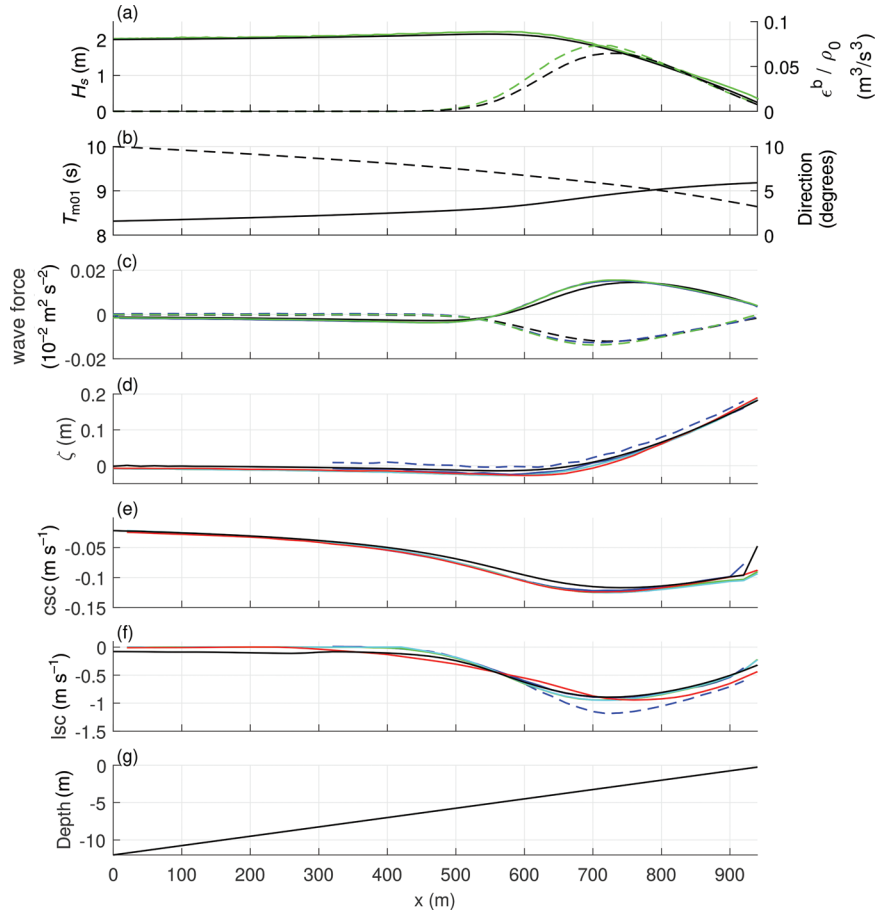
Figure 2. The Planar beach test case: Our results (black) are compared with Haas and Warner (2009; blue), Uchiyama, McWilliams, and Shchepetkin (2010; green), and Michaud et al. (2012; red). (a) H_s (solid) and ϵ^b/ρ_0 (dashed), (b) T_{m01} (solid) and wave direction (dashed), (c) wave-induced forcing in x (solid) and in y (dashed), (d) wave set-up, (e) cross-shore current (csc) velocity, (f) alongshore current (lsc) velocity, and (g) wave-averaged water depth. In (c) all the values for y-direction are scaled up by 10 for plotting.

to shore-normal. The power m $=$ 200 is chosen for the directional distribution function $\cos^m(\theta - \theta_{peak})$ which results in a narrow spectrum in directional domain. We found the choice of such narrow directional spectrum necessary in order to reproduce the same dissipation function as reported by Uchiyama, McWilliams, and Shchepetkin (2010). The evolution of the significant wave height, wave angle and mean wave period are shown in Figure 2(a and b). The dissipation function is presented in Figure 2(a). The wave-induced force (calculated here using the radiation stress gradient) is presented in Figure 2(c). Wherever available, the

results from Haas and Warner (2009), Uchiyama, McWilliams, and Shchepetkin (2010), and Michaud et al. (2012) are given for comparison.

This test was first proposed by (Haas and Warner 2009) Their initial objective was to compare the quasi-3D nearSHORE CIRCulation model (SHORECIRC) of Svendsen, Haas, and Zhao (2002) and the Regional Ocean Modeling System (ROMS). SHORECIRC, Haas, and Zhao includes the vertical variation of current within a depth integrated model. ROMS on the other hand is a fully three-dimensional circulation model. Haas and Warner used the ROMS version modified by Warner et al. (2008) to include wave effects on the current field based on a set of wave averaged equations derived by Mellor (2003, 2005). Both models use the radiation stress gradient formulation to calculate the wave-induced forcing.

In the work of Haas and Warner (2009), both of the hydrodynamic models use an along-shore periodic lateral boundary condition. One-way coupling is used from wave model to hydrodynamic model. Haas and Warner show relatively good fitting of the two models used. Their results are presented Figure 2(d, e and f). The depth profile is shown in Figure 2(g).

The quadratic bottom drag law of Svendsen and Putrevu (1990) is used to calculate the effective bottom shear stress τ_b^e in COHERENS.

$$\boldsymbol{\tau}_b^e = \rho_0 C_D |\bar{\bar{\boldsymbol{u}}}| \hat{\boldsymbol{u}}_b. \tag{13}$$

Where $\hat{\boldsymbol{u}}_b$ is the horizontal velocity at the bottom-most grid cell in the three-dimensional simulations and the depth-averaged horizontal velocity ($\bar{\bar{\boldsymbol{u}}}$) in the two-dimensional barotropic cases. $C_D = 0.0015$ is the bottom drag coefficient.

Uchiyama, McWilliams, and Shchepetkin (2010) used exactly the same settings for the test as was used earlier by Haas and Warner (2009). The only differences were that: (1) they used an alternative wave forcing calculation based on the breaking dissipation formulation by Thornton and Guza (1983) as compared with the standard SWAN formulation of Battjes and Janssen (1978) in Haas and Warner, and (2) they used another version of ROMS with the vortex force formulation of McWilliams, Restrepo, and Lane (2004).

(Uchiyama, McWilliams, and Shchepetkin (2010, fig, 16[a]) also presented the dissipation function obtained from the wave model. Their result for the dissipation function is presented together with the results from this study in Figure 2(a). The wave-induced forcing they obtained using the dissipation function is shown in Figure 2(c). Uchiyama, McWilliams, and Shchepetkin ran a two-dimensional barotropic case with depth-averaged velocities and three three-dimensional cases, though we have included here only the results of their barotropic test for comparison.

For an alongshore uniform and steady test case (neglecting Coriolis forcing because of the small area involved) Uchiyama, McWilliams, and Shchepetkin (2010) derived the analytical solutions. Of interest,

$$\bar{\bar{u}} = -\bar{U}_s. \tag{14}$$

They also derived an analytic solution for the alongshore velocity by balancing the bottom shear stress and wave-driven force in the direction parallel to the coastline.

$$\rho_0 C_D |\bar{\hat{u}}| \bar{\hat{v}} = \frac{\epsilon_{br} k_y}{\sigma} \tag{15}$$

Also for the cross-shore profile of wave-induced set-up, they derived an analytic approximation by integrating the cross-shore component of wave-induced force from the offshore boundary to the coastline.

$$g \frac{\partial \hat{\zeta}}{\partial x} \approx \frac{\epsilon_{br} k_x}{\rho_0 \sigma D} \tag{16}$$

Figure 2 shows the analytic results for wave set-up, cross-shore current and alongshore current.

Michaud et al. (2012) applied this test case by coupling the SYMPHONIE three-dimensional circulation model from the Sirocco system group (Marsaleix et al. 2008; Marsaleix, Auclair, and Estournel 2009) with SWAN. SYMPHONIE uses the glm2 theory of Ardhuin, Rascle, and Belibassakis (2007) as formulated by Bennis, Ardhuin, and Dumas (2011). The results obtained by Michaud et al. (2012) are included in Figure 2(d-f).

Apart from some minor differences, the overall setup of simulations for Haas and Warner (2009), Uchiyama, McWilliams, and Shchepetkin (2010), and Michaud et al. (2012) are similar. These minor differences include the wetting/drying approach, boundary conditions, and velocities used for bottom stress calculation. Some of the abovementioned tests use a wetting/drying scheme, whereas others use wall boundary with minimum depth. Haas and Warner (2009) use depth-averaged velocities for calculation of bottom stress in both ROMS and SHORECIRC. Uchiyama, McWilliams, and Shchepetkin (2010) use depth-averaged velocities in two-dimensional cases and the bottom-most grid cell velocities in three-dimensional cases. Michaud et al. (2012) also use the bottom-most grid velocities. As stated earlier, we also use depth-averaged velocities. However, these differences do not play an important role in the results.

In all cases, Coriolis force, wave roller effects, momentum diffusion and current effect on waves are ignored.

We have tested our coupled set of COHERENS-SWAN on this case. COHERENS is running in barotropic mode. For SWAN, we use cyclic boundary condition. With this option, the flux that exits the domain from the eastern boundary enters the domain from the western boundary and vice versa. This option in SWAN works only in the east-west direction. Therefore, in order to use this boundary condition, the whole domain orientation was rotated $90°$ in our experiment. Nevertheless, in the figure captions and axis labels, the original $x - y$ orientation of Haas and Warner (2009) is maintained to avoid confusion. In SWAN we included bottom friction, depth-induced breaking, and white-capping. However, the latter is expected to be negligible in this case. We excluded nonlinear wave-wave interaction and wind forcing for this test case. We used the backward in space backward in time

(BSBT) propagation method in SWAN. In the spectral discretization in SWAN we use 90 directional bins of 4° and 30 frequency bins with a minimum of 0.04 Hz and a maximum of 0.5 Hz.

A comparison of wave results obtained here and from Haas and Warner (2009); Uchiyama, McWilliams, and Shchepetkin (2010); Michaud et al. (2012) is given in Figure 2. They show very close agreement for H_s, ϵ_{br}/ρ_0, F_x^w and F_y^w. As shown in Figure 2(c), there is a slight underestimation in the wave-induced forces in our result compared with the ones of Uchiyama, McWilliams, and Shchepetkin (2010). This is most likely due to lower wave dissipation rate. If bottom friction is not used in the wave model, we obtain a higher wave dissipation rate due to breaking (not shown here). In that case the results are closer to the ones of Uchiyama, McWilliams, and Shchepetkin (2010). As it can be seen in Figure 2, the wave set-up simulated in all four experiments are almost identical. Our results for cross-shore velocity show undertow equal to the depth-averaged return mean flow, which is driven by the prevailing undertow (Fig. 2(e)). The along-shore velocity is also identical to the analytic solution (Eq. 15). Both of the cross-shore and alongshore velocities fit well with results obtained by others.

b. Single-barred beach

In cases with a bar in the breaking zone which is a common system in coastal waters, the sharp gradient of wave-induced momentum and bottom stress can result in shear instabilities with eddies fluctuating periodically alongshore (Uchiyama, McWilliams, and Restrepo 2009). The objective of this test case is to reproduce dynamically wave effects such as undertow, set-up, set-down and alongshore current.

The rectangular Cartesian domain of the test is 512 m wide in x-direction (positive eastward) and 768 m long in y-direction (positive northward). The cross-shore dimension (512 m) is chosen equal to about 4 times the width of the surf zone. The alongshore dimension (768 m) is chosen about 6 to 8 times the wavelength of shear waves in the marginally unstable regime (Uchiyama, McWilliams, and Restrepo 2009). The bar is situated at the distance of 100 m from the shoreline of the beach with uniform slope of 1:50. The depth starts at 10 m offshore at x = 0. The bottom topography is illustrated in Figure 3(g). The incident waves are obtained by combining a JONSWAP spectrum ($H_s = 1.414$ m, $T_p = 10$ s, $\theta_p = 10°$ with respect to shore-normal with power m = 200 for directional spreading function), which results in a very narrow (directional) wave spectrum.

The quadratic bottom drag law (Eq. 13) with a constant bottom drag coefficient of $C_D = 0.0015$ is used in COHERENS to calculate the effective bottom shear stress. For SWAN, we included the bottom friction, depth-induced wave breaking and white-capping. We ignored the wind input and nonlinear wave-wave interaction. The spectral discretization in SWAN is the same as in the planar beach test case.

This single-barred beach test case is adopted by McWilliams, Restrepo, and Lane (2004) from previous works of Longuet-Higgins and Stewart (1962) and Özkan-Haller and
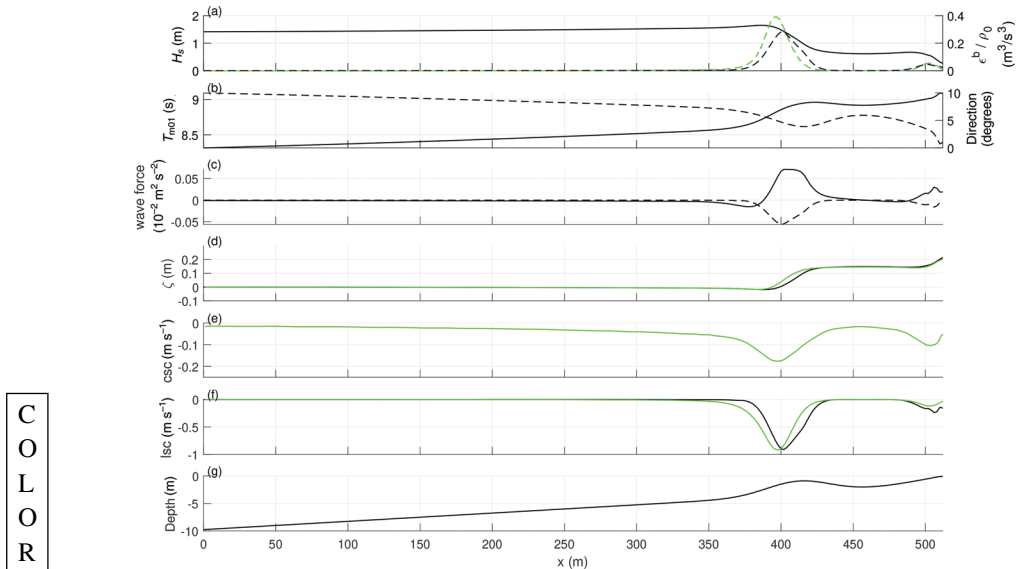
Figure 3. The barred beach test case: Our results (black) are compared with Uchiyama, McWilliams, and Restrepo (2009; green). (a) H_s (solid) and ϵ^b/ρ_0 (dashed), (b) T_{m01} (solid) and wave direction (dashed), (c) wave-induced forcing in x (solid) and in y (dashed), (d) wave set-up, (e) cross-shore current (csc) velocity, (f) alongshore current (lsc) velocity, and (g) wave-averaged water depth. In (c) all the values for y-direction are scaled up by 10 for plotting.

Li 2003. Uchiyama, McWilliams, and Restrepo (2009) used this test in a setting with the asymptotic theory of McWilliams, Restrepo, and Lane (2004). They used the resulting barotropic wave-averaged quasi-Eulerian model to simulate wave set-up and set-down as well as littoral current. The quasi-static response they obtained was due to conservative effects of wave separated from the non-conservative set-up Uchiyama, McWilliams, and Restrepo 2009, fig. 2[a]). The sum of their results for quasi-static response and set-up are shown in Figure 3(d). The wave shoaling and the dissipation of wave energy due to breaking are given in Figure 3(a). The wave propagation angle and mean wave period (Fig. 3[b]) show the refraction with the sharp gradient around the position of the bar. The wave-induced force is presented in Figure 3(c). The forcing is calculated here as radiation stress gradient.

As can be seen in Figure 3, the results obtained from our model include both set-up and set-down and fit reasonably well with those obtained by Uchiyama, McWilliams, and Restrepo (2009). Also the cross-shore and alongshore velocities obtained in our study correspond well with those of Uchiyama, McWilliams, and Restrepo (2009). As in the planar beach case, the wave dissipation rate obtained is slightly lower than in Uchiyama, McWilliams, and Restrepo (2009), but the dissipation rates were estimated by two different formulations (see Section 4a).

In summary, from the results of the academic test cases of planar beach and single-barred beach, we conclude that the COHERENS-SWAN coupled set performs well in reproducing wave-induced currents and set-up in the depth-averaged mode.

5. The Belgian coast

a. The idealized one-dimensional test

We developed this test in response to the conditions posed by the multiple sand bars in the southern North Sea. This semi-realistic test case makes it possible to examine whether other processes play a role in a setting with realistic wave spectra and in a domain that stretches from intermediate depth to shallow waters.

This area is characterized by multiple tidal sandbanks. These banks belong to the category of open shelf ridges and are oriented to the angle of the tidal flow (Franzetti et al. 2015). Some are nearly parallel to the coastline and are situated in the intermediate to shallow waters. Others stretch back to deeper waters. The hydrodynamic system in this area is to a large extent dominated by tidal currents (Deleu et al. 2004). The strong tidal currents, along with the wind-wave enhancement of bed stress, are believed to be the main factors affecting the shape and orientation of these tidal sandbanks (Huthnance et al. 2016). Additionally, the wave energy dissipation in the intermediate and to a greater degree in the shallow areas affects the wave regime in this area.

The bathymetry of the Belgian coastal area is shown in Figure 4. A depth profile roughly perpendicular to the coastline is distilled from the bathymetric data. The profile starts offshore at a distance approximately equal to the distance from the coastline to the location of the Westhinder (WHI) wave observation station. Observations from this station are often used as boundary condition for coastal model studies. The resulting depth profile is shown in Figure 5(g).

The rectangular Cartesian domain of the test is 35,700 m cross-shore in x-direction (positive eastward) and 200 m alongshore in y-direction (positive northward). The Δx is chosen equal to 100 m and the Δy is chosen equal to 20 m.

The measured wave spectrum at WHI on 12 February 2005 at 14:00 h with $H_s = 4$ m, $T_{m01} = 7$ s and incident angle of about 20° with respect to shore-normal is applied at the offshore western boundary of SWAN. The northern and southern boundary conditions in SWAN are assumed as cyclic boundary conditions. For the sake of simplicity the COHERENS-SWAN results have been converted to the coordinate system used in the previous tests. In COHERENS, zero volume flux boundary condition is applied at all open boundaries. Astronomical tide, wind input, and inverse barometric effect are ignored. Similar to the academic test cases, the quadratic bottom drag law of Svendsen and Putrevu (1990) is used with the constant bottom drag coefficient of $C_D = 0.0015$.

The SWAN simulation results show that as the waves propagate toward the coast, refraction reduces the incident angle from 20° to almost 0° at the shoreline. As shown in Figure 5(a), the waves shoal as they approach each of the bars. The total dissipation function
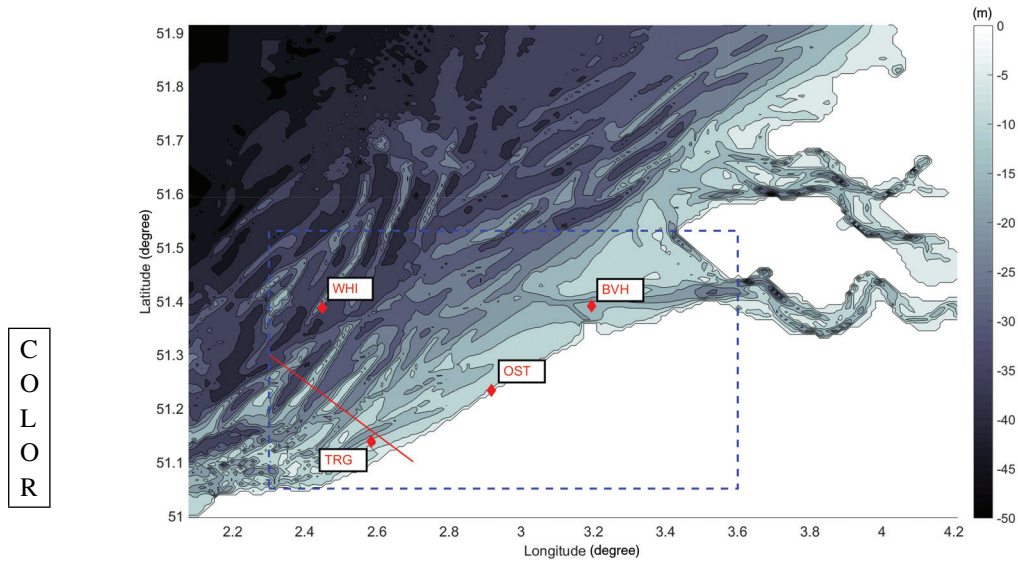
C
O
L
O
R

Figure 4. The Belgian coast bathymetry with the position of the profile line in red. The domain of the 2D test case is shown with dashed blue line. Red diamonds identify stations: Westhinder (WHI), Bol Van Heist (BVH), Ostende (OST), and Trapegeer (TRG).
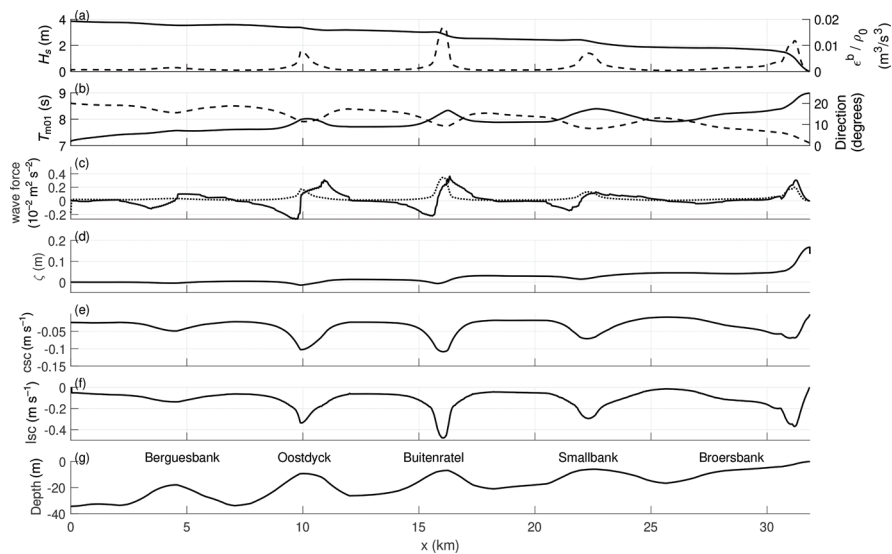

Figure 5. The Belgian coast, one-dimensional test. (a) H_s (solid) and ϵ^b/ρ_0 (dashed), (b) T_{m01} (solid) and wave direction (dashed), (c) wave-induced forcing in x- (solid) and in y- (dashed) direction, (d) wave set-up, (e) cross-shore velocity current (csc) velocity, (f) alongshore velocity, and (g) wave-averaged water depth. In (c) all the values for y-direction are scaled up by 10 for plotting. The names of the tidal banks are given (g).

as output from SWAN is also given. The wave energy goes through five peaks of dissipation, one on each of the four bars and the last on the shore.

The wave-induced force calculated as radiation stress gradient is shown in Figure 5(c).

Figure 5 also shows the response of the circulation model. Figure 5(d) shows the combination of wave-induced set-up and set-down. At the shoreline, the set-up reaches up to 17 cm. A relative drop of the water surface (set-down) occours slightly in front of each bar. Figure 5(e) gives the cross-shore current, or undertow, which is equal to the depth-averaged return mean flow. Figure 5(f) shows the alongshore current. The along-shore current with maximum of 0.4 m s^{-1} fits relatively well with the analytic solution.

b. The two-dimensional real test case

Up to this point, the coupled set has been successfully validated against academic test cases. The order of magnitude of the currents and the set-up expected from the wave forcing is illustrated in the one-dimensional case (Section 5a). In this section, we use the coupled set in a practical two-dimensional case of the Belgian coast (bc2d).

i. The domain, grid, and bathymetry. The chosen domain of bc2d covers the Belgian coastal area and is situated in the southern North Sea. It stretches in longitude from 2.3° E to 3.6° E (roughly equal to 94 km) and in latitude from 51.05° N to 51.5° N (roughly equal to 53 km). The grid is Cartesian rectangular with mesh sizes equal to 500 m in *x*- and *y*-directions. Figure 6 presents the bathymetry and the domain of the bc2d grid.

ii. The wave and hydrodynamic boundary conditions. To study the hydrodynamic and wave condition in the southern North Sea, a system consisting of six grids is assembled. This system contains three nested runs for circulation modeling and three nested runs for wave modeling. Figure 7 presents the layout of this system and the area covered in each grid.

In the hydrodynamic-model (shown on the left side of the figure), in the coarsest grid (OPTOS-CSM), the COHERENS circulation model is driven by the main eight tidal constituents at the boundaries. This simulation produces the boundary conditions for the intermediate grid (OPTOS-NOS). The results of the intermediate grid produces the boundary condition for the fine grid (OPTOS-BCZ). Finally, the simulation on the fine grid (OPTOS-BCZ) provides the hydrodynamic boundary condition for bc2d grid. Meteorological forcing is included through atmospheric pressure and wind velocities at 10 m in all of the hydrodynamic simulations (European Centre for Medium-Range, Weather Forecasts [ECMWF], Era-Interim, 6-hourly, and spatial resolution of 0.125°; [Dee et al. 2011]). A constant bottom roughness length of $z_{0b} = 0.0035$ is assumed throughout this case study.

In the coarsest grid (C_24) for the wave-model (shown on the right side of Figure 7), Wave Advanced Model (WAM) Cycle 4.5.3 is driven by wind velocity. This simulation produces the boundary condition for the intermediate grid (N1_24). At the intermediate level (N1_24), WAM uses water level and current velocities obtained from COHERENS
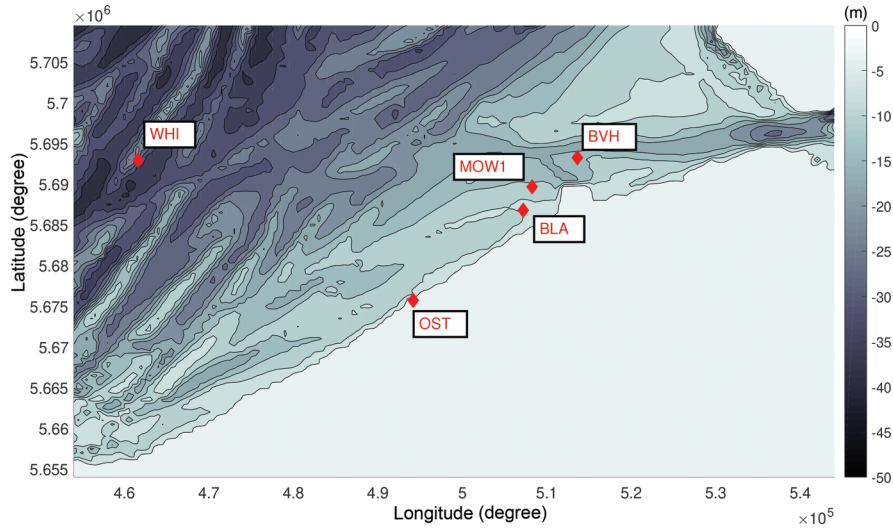
Figure 6. The domain and bathymetry of the 2D test case. The position of the measurement stations (Westhinder [WHI], MOW1, Bol Van Heist [BVH], Blankenberge [BLA], and Ostende [OST]) is also shown.
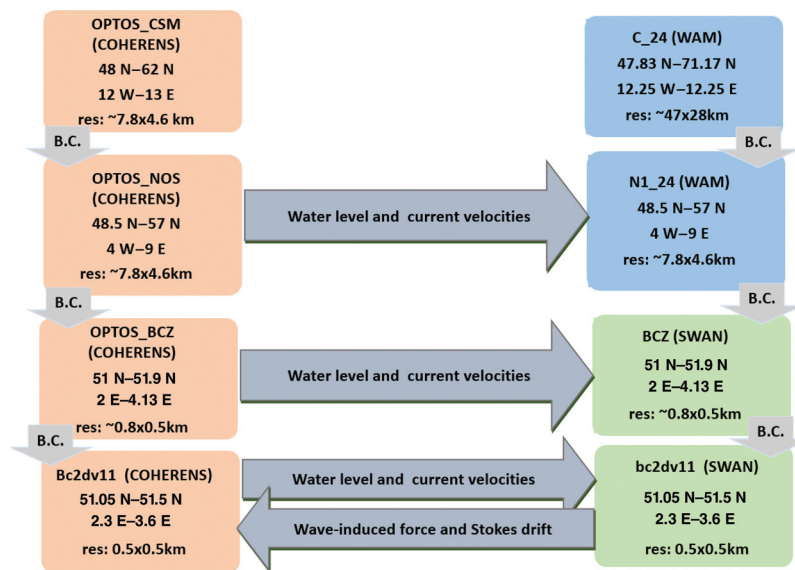

Figure 7. The layout of the six grids nested system used to drive the wave and hydrodynamic boundary condition for the 2D test case. The two grids used for WAM (C_24 and N1_24) are very similar to those used for COHERENS (respectively, OPTOS_CSM and OPTOS_NOS). The down arrows show that the boundary condition (B.C.) is provided for the finer grid. The name bc2dv11 refers to the last version of the Belgian coast 2D (bc2d) grid.

to account for one-way coupling of current effects on waves. The results of WAM on the N1_24 grid provide the boundary condition for the fine grid (BCZ). For the simulation on BCZ grid, the SWAN wave model is used. At this level, SWAN version 40.91 (http://swanmodel.sourceforge.net) uses the information of water level and current velocities obtained from COHERENS through an online information exchange to account for one-way current on wave effects. The SWAN simulation on BCZ provides the boundary condition data (two-dimensional wave energy spectra on 20 points) for the run on bc2d grid. The wind energy input is taken into account in all of the wave simulations by WAM and SWAN.

iii. The measurements. The current velocity measurements are the results of multiple measurement campaigns (Baeye et al. 2012). During these campaigns an acoustic Doppler profiler (ADP) was mounted at the Blankenberge (BLA) and MOW1 stations from 13 February 2006 to 5 June 2008. MOW1 is a measuring pole (number 1) of the Department of Mobility and Public Works of the Flemish Government Departement Mobiliteit en Openbare Werken van de Vlaamse Overheid). The positions of these points are presented in Figure 6(b). The BLA measurement station is at a depth of 5 m MSL and the MOW1 station at a depth of 9 m MSL. The ADP is deployed facing downwards at 2.3 m from bottom. The resulting velocity includes west-east and south-north components of current velocities at every 25 cm of depth in the lowest 2.3 m of water column. These values are then averaged to get the average velocity of the lowest 2.3 m of water column. The outcome is then assumed representative for the depth-averaged mean flow over the whole water column. We chose for the BLA station because it has lower depth.

To compare with the modeled velocities, the measured velocity components were projected onto an alongshore cross-shore orthogonal coordinate system assuming 30° counterclockwise orientation of the Belgian coastal line with respect to a west-east axis. The positive direction of the alongshore axis is oriented roughly to the northeast and the positive direction of the cross-shore axis is directed offshore, roughly towards the northwest.

Though the assumed outcome mentioned above might give velocities lower than the real depth-averaged velocity, it is made on the basis of the only available measurements taken in the area, and it enables us to make a meaningful estimation of nearshore current velocities for comparison with modeled results. This assumption is more tricky in case of the cross-shore current as we would expect that the average cross-shore velocity of the lowest 2.3 m of water column could contain the undertow. However, as (Baeye et al. 2011, fig. 4) and (Baeye et al. 2012, fig. 11) showed, the measured alongshore and cross-shore velocities at the depth of 1.25 m above the bed contain both the ebb and the flood signal. In both cases of alongshore/cross-shore velocities, we see positive values as well as negative values in the same order of magnitude.

Among the obtained current measurements, the two stormy periods of January 2007 (shore-parallel waves; Fig. 8 and Fig. 9) and March 2008 (shore-normal waves; Fig. 10 and Fig. 11) were selected for simulations. The water level measurements used in Figure 9 and Figure 11 are obtained from the measurement station in Ostende (OST). The measured
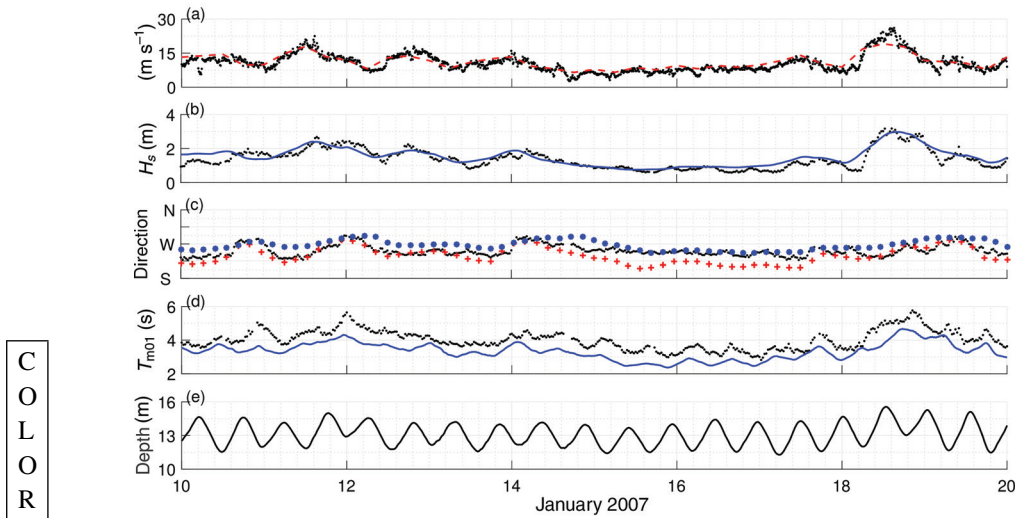
Figure 8. January 2007 storm observations and model correlations. (a) wind velocity (observation in dotted black and ECMWF in dashed red), (b) H_s (observation at BVH in dotted black and SWAN results in blue), (c) direction (observed wave direction at BVH in dotted black; SWAN results for wave direction in blue * and ECMWF for wind direction in red +), (d) T_{m02} (observation at BVH in dotted black and SWAN results in blue), and (e) total water depth (COHERENS).
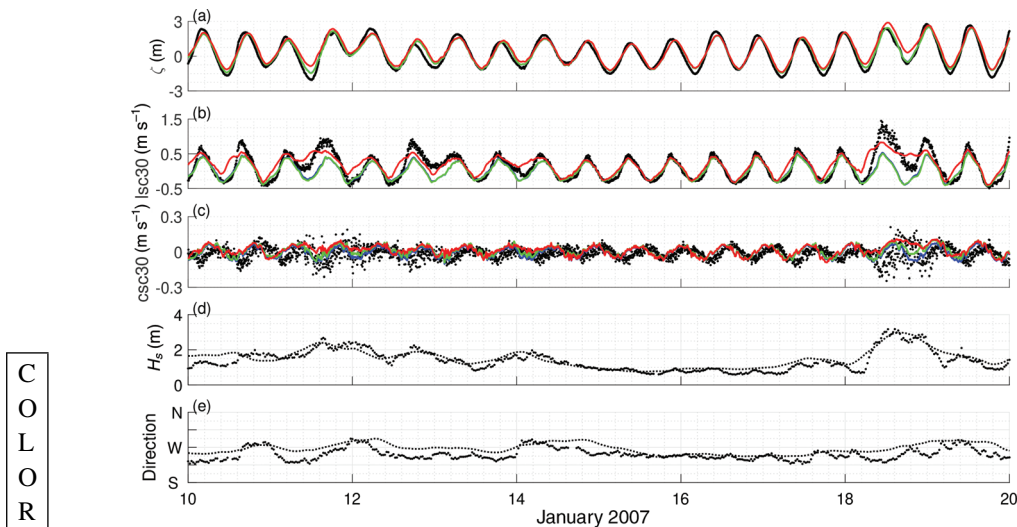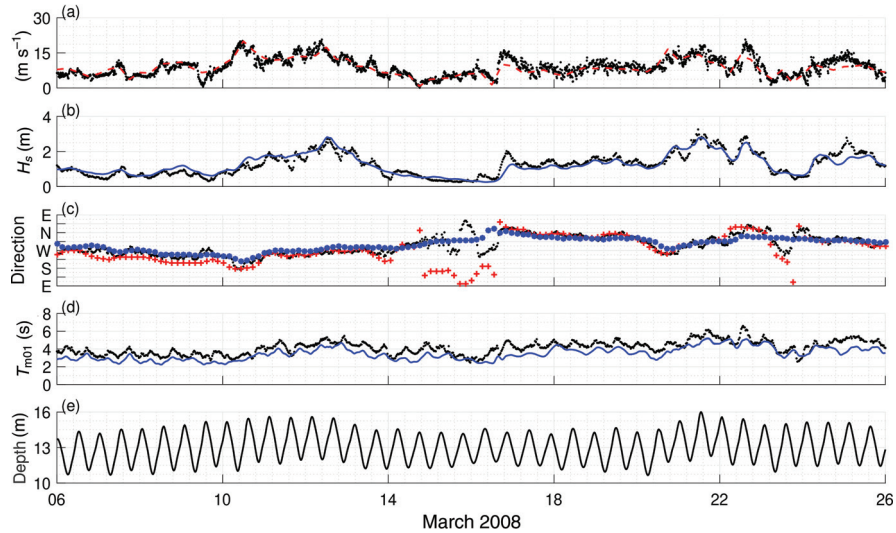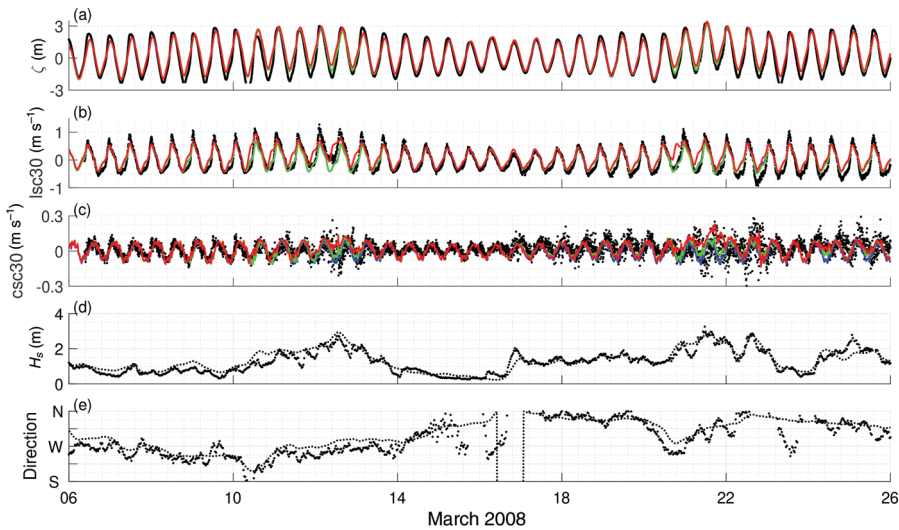

Figure 9. January 2007 storm observations and simulated runs. (a) water level at Ostende (OST) station, (b) alongshore current (lsc) at Bol Van Heist (BVH), (c) cross-shore current (csc) at BVH, (d) H_s and (e) wave direction, both at BVH. In (a-c), the observed (black), run a simulation (blue), run b simulation (green), and run c simulation (red). In (d) and (e), the observation (bold dotted) and SWAN results (dotted).

Figure 10. March 2008 storm observations and model correlations. (a) wind velocity (observation in dotted black and ECMWF in dashed red), (b) H_s (observation at Bol Van Heist [BVH] in dotted black and SWAN results in blue), (c) direction (observed wave direction at BVH in dotted black, SWAN results wave direction in blue * and ECMWF wind direction in red +), (d) T_{m02} (observation at BVH in dotted black and SWAN results in blue), and (e) total water depth (COHERENS)

Figure 11. March 2008 storm observations and simulated runs. (a) water level at Ostende (OST), (b) alongshore current (lsc) at Bol Van Heist (BVH), (c) cross-shore current (csc) at BVH, (d) H_s and (e) wave direction, both at BVH. In (a-c) the observed (black), run a simulation (blue), run b simulation (green), and run c simulation (red). In (d) and (e), the observation (bold dotted) and SWAN results (dotted).

significant wave height given in those figures is obtained from the directional wave buoy at Bol Van Heist (BVH). The positions of these stations are illustrated in Figure 6(b).

iv. The simulation and results. For each of the two abovementioned storms, we look at three different simulations on the bc2d grid:

- run a: COHERENS model alone

    The COHERENS model is derived by the hydrodynamic boundary condition obtained from the OPTOS_BCZ fine grid run (see Figure 7). In this simulation, the wave influence on the currents is ignored. The results of COHERENS from run a are expected to resemble the tide and meteorological forcing (wind drag and inverse barometer effects).

- run b: COHERENS-SWAN coupled set (radiation stress gradient theory)

    In this simulation, we use the data obtained from the six-grids setup as the boundary condition for SWAN and COHERENS. The wave boundary condition is applied as two-dimensional wave energy spectra on 20 points spread along the west and north side of the domain. The coupling is in two ways. The water level and current velocity vector are passed from COHERENS to SWAN and the wave-induced force and the depth-averaged Stokes drift are passed from SWAN to COHERENS. In this run b, the wave induced force is calculated as the gradient of waves' radiation stress (see Eq. 7).

- run c: COHERENS-SWAN coupled set (dissipation theory)

    This simulation on bc2d grid is very similar to run b. The only difference is that in this run, the wave induced force is calculated using the dissipation theory (see Eq. 9).

For each of the two storms, the results from the wave model are illustrated in Figure 8 and Figure 10. It is clear from Figure 8(c), that the dominant regime of the storm of Januray 2007 is southwesterly during both storm peaks with wave period T_{m02} fluctuating around 4 s. As Figure 10(c) shows, the dominant regime for the storm of March 2008 is westerly during the first storm peak (10–14 March) and northerly during the second storm peak (22–23 March). The wave period T_{m02} fluctuates around 5 s during the storm of March 2008.

The resulting time-series for water level, alongshore current velocity (lsc30), and cross-shore current velocity (csc30; assuming 30° coastline orientation) are illustrated in Figure 9 and Figure 11 for all of the three simulations mentioned above.

To determine the relative efficacy of the two methods of calculation of wave-induced force (i.e., radiation stress gradient and wave dissipation) in improving the hydrodynamic simulation, we compare the statistical indicators for each run with the observations for the time-series of water level, alongshore velocity, and cross-shore velocity (i.e., the N values long set of observed values $[\hat{y}^t]$ at time instants $[t]$ against the set of corresponding simulated values $[y_t]$ at the same t. We look at the following indicators:

- The bias is calculated as

$$bias = \frac{\sum\limits_{t=1}^{T}(\hat{y}_t - y_t)}{T}.$$ (17)

- The root mean square error (RMSE) is calculated after removing the bias as

$$RMSE = \sqrt{\frac{\sum\limits_{t=1}^{T}(\hat{y}_t - y_t - bias)^2}{T}}.$$ (18)

The RMSE parameter is always positive with a value of 0 referring to the perfect match between simulation and observation.

- The linear regression index is calculated as

$$R^2 = 1 - \frac{\sum\limits_{t=1}^{T}(\hat{y}_t - y_t)^2}{\sum\limits_{t=1}^{T}(\hat{y}_t - \overline{\hat{y}}_t)^2}.$$ (19)

In equation 19 we have used $\overline{\hat{y}}_t$ to denote the value averaged over the whole data set $\overline{\hat{y}}_t = \frac{\sum\limits_{t=1}^{T}(\hat{y}_t)}{T}$. R^2 can be used as a measure of the extent to which the model is successful in forecasting the observation. It has a minimum of 0 and a maximum of 1, which corresponds to a perfect situation.

- The skill score (SS) is calculated using the RMSE as

$$SS = 1 - \frac{RMSE}{\sigma_{obs}}.$$ (20)

Where σ_{obs} refers to standard deviation of the observation. The SS parameter equal to 1 refers to a perfect forecast.

Table 2 presents the statistical parameters (i.e., water level and alongshore and cross-shore velocities) used for quantitative comparison of runs a, b, and c for the two stormy periods of 2007 and 2008. To draw a conclusion from the presented statistical indicators in Table 2, we need to compare for every simulated parameter and every storm the values of run b and run c with the values of run a, since run a is the bench simulation. The values for csc30 are not very indicative, as many of the statistical parameters fall outside the expected range because of the

Table 2. The performance of the model for two stormy periods, showing parameters and statistical indicators for each simulation. Parameters are water level, alongshore current (lsc), and cross-shore current (scs). Statistical indicators are root mean square error (RMSE), bias, linear regression index (R^2), and skill score (SS).

Storm	Parameter	Run	RMSE	Bias	R^2	SS
6–24 March 2008	water level	a	0.42	−0.17	0.91	0.69
		b	0.42	−0.17	0.91	0.69
		c	0.45	−0.24	0.88	0.65
	lsc30	a	0.18	−0.02	0.81	0.56
		b	0.17	−0.01	0.82	0.57
		c	0.19	−0.09	0.74	0.49
	csc30	a	0.06	0.02	−0.18	−0.06
		b	0.06	0.00	−0.02	−0.01
		c	0.07	0.00	−0.19	−0.09
10–20 January 2007	water level	a	0.31	−0.07	0.93	0.73
		b	0.31	−0.07	0.93	0.73
		c	0.37	−0.21	0.87	0.64
	lsc30	a	0.21	0.11	0.58	0.35
		b	0.21	0.12	0.55	0.33
		c	0.19	−0.06	0.70	0.45
	csc30	a	0.06	−0.01	−0.29	−0.14
		b	0.06	−0.02	−0.44	−0.20
		c	0.06	−0.03	−0.74	−0.32

high range of fluctuations in csc30; we, therefore limit ourselves to a qualitative comparison. For lsc30, however, we see systematic improvements of all statistical indicators for run b for the storm of March 2008. In the case of the storm of January 2007, we see improvements for lsc30 for run c. This is due to these two storms having different dominant incident angles.

The storm of January 2007 is roughly parallel with the coastline. Two distinct storm peaks can be identified: the first one on 12 January and the second one on 19 January. The wave direction during both peaks follows perfectly the wind direction but is turned a bit more shore-normal, which can be attributed to refraction effects. The effect of currents on waves from the tidal modulation of T_{m02} is clearly shown in Figure 10(d). For southwesterly wind conditions, one can expect fetch limited conditions and therefore considerable wave dissipation through white-capping and limited wave dissipation due to wave breaking. We examine this hypothesis by looking at the dissipation functions of SWAN along a shore-normal section starting at deeper water and going through the BLA station.

During the storm of March 2008 two distinct storm peaks can be identified: first one on 13 March and the second one on 23 March. The wave direction during the first storm peak is

westerly. In contrast the wave direction during the second storm peak is northerly (roughly shore-normal).

We present the results from the coupling set for runs a, b, and c in Figure 9 for the storm of January 2007. The two storm peaks cause anomalies in the water level and current velocities (Fig. 9[a–c]). The results from SWAN run b are almost identical to run c. For ease of comparison, these two panels (Fig. 8[b–c]) are repeated in Figure 9(d–e). The first storm peak lasts about one full day (11 January, 03:00 h until 12 January, 03:00 h) or two tidal loops. In figure 9 panel a, the effects of this storm on the water level can be seen as an overall increase in water level (surge). In this panel we do not see any clear or consistent improvement of simulated water level for runs b and c during the storm peaks. We notice that in the water level time-series, the initial run a (no wave-current interaction included) simulates the surge conditions during the storm peaks very well.

In lsc30, we see an abnormal increase on the rising side of the tidal loop (11 January, 12:00 h). Note that this is when the direction of lsc30 is the same as the wave direction.

The increase in lsc30 is reflected only in run c. The increase in lsc30 due to wave-induced force during both storm peaks happens only for lsc30 above zero or, in other words, when lsc30 and waves have the same direction.

In figure 9 panel c, we see the storm peaks coinciding with fluctuations in csc30. These fluctuations are also visible in runs b and c. Especially during the second storm peak (18 January, 18:00 h), these fluctuations are visible in run c. However, there is no clear and consistent improvement in the calculated cross-shore current. This is not surprising given that we expect the wave induced cross-shore current will be relatively small. Moreover we are looking here at depth-averaged currents and in the case of undertow, the measured cross-shore current velocities might not be representative for the depth-averaged velocity.

The results from the coupling set for runs a, b, and c for the storm of March 2008 are presented in Figure 11. As this figure shows, the first storm peak (on 13 March) is a westerly storm. As with the storm peaks of January 2007, the dissipation approach gives better results in hindcasting wave-induced effects on along-shore currents (see Fig. 11[b]). Whereas in the case of the second storm peak (on 23 March), which is a northerly storm (roughly shore-normal), the radiation stress gradient and dissipation approaches give similar results. As can be seen in Figure 11(a), the hydrodynamic model simulates the wind surge quite effectively. However, including the wave-induced force does not improve the simulation results for water level. As Figure 11(c) shows, the fluctuations in cross-shore current during the storm peaks are considerably higher in the case of the second storm peak (shore-normal storm) in comparison with the first storm peak (shore-parallel). As with the case of January 2007, it is hard to draw meaningful conclusions by comparing the simulated and observed cross-shore currents because the measured cross-shore current velocity might not be representative for the depth-averaged velocity. However, the inclusion of the wave-induced force and Stokes drift does improve the simulation results regarding the order of magnitude of these fluctuations.

6. Concluding remarks and future work

Some of the effects of wind-induced waves on the mean flow have been examined. The COHERENS hydrodynamic model and the SWAN spectral wave model have been coupled. The existing methods for calculation of wave-induced force on the mean flow based on (1) radiation stress gradient and (2) wave dissipation are implemented and compared.

Two existing academic test cases, were used for validation. The results of these two simplified tests compare well with the literature Haas and Warner 2009; Uchiyama, McWilliams, and Restrepo 2009; Uchiyama, McWilliams, and Shchepetkin 2010; Michaud et al. 2012) and verify the sound functionality of the coupled set.

In order to investigate the wave effects on the mean flow in a coastal area with multiple bars, a semi-realistic one-dimensional test has been worked out. The proposed test makes it possible to examine the wave effects in a rather simplified situation. This test enables us to keep the division between wave effects on alongshore direction and on cross-shore direction similar to the previous academic test cases. Furthermore, this test enables us to examine the order of magnitude of the response expected from the hydrodynamic system to wave-induced forcing in the studied area.

Finally, a two-dimensional test case based on the Belgian coastal waters is presented. By hindcasting two stormy periods (with four storm peaks in total) with wave direction roughly parallel to the coastline during three of the storm peaks and wave direction roughly normal to the coastline during one of the storm peaks, the improvements of simulation results after taking into account the wave effects is shown. More specifically, it is shown that including the wave sources of momentum and mass in the hydrodynamic model can improve the simulation of alongshore current significantly. We also show clearly that for the storms roughly parallel to the coast, calculating wave-induced force using the dissipation method gives much better results than using radiation stress gradient. We also show that in the case of a shore-normal storm, the two methods perform similarly. For the particular case of shore-parallel waves, white-capping dissipation is the dominant dissipation source term in contrast to more shore-normal wave conditions (e.g., the second storm peak of March 2008) in which depth-induced breaking is dominant. In the former, the energy dissipation in the wave spectrum is balanced with wind input growth and does not result in a gradient of the radiation stresses. This test case therefore, demonstrates that using wave dissipation for coupling with the hydrodynamic model is more consistent and more general than using the radiation stress gradient approach, even in the depth-averaged mode. This is because under strong wind conditions parallel to the coastline, the wave-induced force due to white-capping dissipation is not properly taken into account in the radiation stress gradient approach.

Future work will include coupling in three dimensions and a search for measurements during wave conditions suitable for exploring in greater detail the effects of wave-current interaction. Having a two- and a three-dimensional model will also help to set-up appropriate measurement campaigns.

Appendix

List of symbols used with their description and unit

Symbol	Description	Unit
(x, y, z)	the Cartesian coordinate system	m
(x^*, y^*, ς)	the σ-coordinate system	m
d	depth of still water	m
$\hat{\zeta}$	local phase-averaged free surface	m
D	total water depth	m
$\hat{\boldsymbol{u}} = (\hat{u}, \hat{v}, \hat{\omega})$	quasi-Eulerian velocity	m s^{-1}
$\boldsymbol{U}_s = (U_s, V_s, W_s)$	near surface wave's Stokes drift	m s^{-1}
$\boldsymbol{U} = (U, V, W)$	Lagrangian velocity	m s^{-1}
$\boldsymbol{F}^w = (F_x^w, F_y^w)$	total wave-induced forcing vector on the mean flow	m^2 s^{-2}
$\boldsymbol{F}_d = (F_{d,x}, F_{d,y})$	wave forcing vector due to near surface dissipation	m^2 s^{-2}
$\boldsymbol{F}_b = (F_{b,x}, F_{b,y})$	wave forcing vector due to near bottom dissipation	m^2 s^{-2}
$\boldsymbol{F}_m = (F_{m,x}, F_{m,y})$	vertical mixing vector	m^2 s^{-2}
C	concentration of passive tracer	kg m^{-3}
ω	modified vertical velocity	m s^{-1}
$\boldsymbol{k} = (k_x, k_y)$	wave number vector	m^{-1}
$\boldsymbol{k}_p$	wave number vector of peak frequency	m^{-1}
p^H	hydrostatic pressure	kg m^{-1} s^{-2}
f	Coriolis parameter	s^{-1}
A	wave amplitude	m
H_s	significant wave height	m
J	wave-induced pressure	m^2 s^{-2}
S	wave's radiation stress tensor	m kg s^{-2}

Symbol	Description	Unit
T_p	peak period	s
$S_{(\mathbf{x},\sigma,\theta,t)}$	the sum of wave energy source and sinks	–
g	gravitational acceleration	m s^{-2}
ρ_0	water density	kg m^{-3}
n	group velocity to phase velocity ratio	–
c_g	wave's group velocity	m s^{-1}
c_{ph}	wave's phase velocity	m s^{-1}
$E_{(\sigma,\theta)}$	the spectral density of surface wave elevation variance	m^2
$N_{(\sigma,\theta)}$	the wave action density	–
θ	wave propagation direction	*rad*
σ	intrinsic wave frequency	s^{-1}
σ_p	the frequency of peak wave energy	s^{-1}
γ	wave breaking constant	–
ϵ_{br}	wave dissipation due to breaking	kg s^{-3}
ϵ_{fr}	wave dissipation due to bottom friction	kg s^{-3}
C_D	bottom drag coefficient	–
$\boldsymbol{\tau}_b^e$	effective bottom shear stress	$\text{kg m}^{-1}\,\text{s}^{-2}$
$\boldsymbol{u}_b$	the horizontal velocity at the bottom-most grid cell	m s^{-1}

REFERENCES

Alves, J.-H., and M. Banner. 2003. Performance of a saturation-based dissipation-rate source term in modeling the fetch-limited evolution of wind waves. J. Phys. Oceanogr., *33*(6), 1274–1298. https://doi.org/10.1175/1520-0485(2003)033<1274:POASDS>2.0.CO;2

Ardhuin, F., N. Rascle, and K. A. Belibassakis. 2007. Explicit wave-averaged primitive equations using a generalized Lagrangian mean. Ocean Model, *20*(1), 35–60. https://doi.org/10.1016/j.ocemod.2007.07.001

Babanin, A. V., A. van der Weshuijsen, D. Chalikov, and W. E. Rogers. 2017. Advanced wave modeling, including wave-current interaction. J. Mar. Res., *75*(3), 239–262. https://doi.org/10.1357/002224017821836798

Baeye, M., M. Fettweis, S. Legrand, Y. Dupont, and V. Van Lancker. 2012. Mine burial in the seabed of high-turbidity area: Findings of a first experiment. Cont. Shelf Res., *43*, 107–119. https://doi.org/10.1016/j.csr.2012.05.009

Baeye, M., M. Fettweis, G. Voulgaris, and V. Van Lancker. 2011. Sediment mobility in response to tidal and wind-driven flows along the Belgian inner shelf, southern North Sea. Ocean Dynam, *61*(5), 611–622. https://doi.org/10.1007/s10236-010-0370-7

Battjes, J. A., and J. P. F. M. Janssen. 1978. Energy loss and set-up due to breaking of random waves. Paper presented at the 16th International Conference on Coastal Engineering, American Society of Civil Engineers, Hamburg, Germany, 27 August–3 September 1978. https://doi.org/10.1061/9780872621909.034

Battjes, J. A., and M. J. F. Stive. 1985. Calibration and verification of a dissipation model for random breaking waves. J. Geophys. Res., *90*(C5), 9159–9167. https://doi.org/10.1029/JC090iC05p09159

Bennis, A.-C., F. Ardhuin, and F. Dumas. 2011. On the coupling of wave and three-dimensional circulation models: Choice of theoretical framework, practical implementation and adiabatic tests. Ocean Model, *40*(3–4), 260–272. https://doi.org/10.1016/j.ocemod.2011.09.003

Bolaños, R., J. M. Brown, and A. J. Souza. 2014. Wave-current interactions in a tide dominated estuary. Cont. Shelf. Res., *87*, 109–123. https://doi.org/10.1016/j.csr.2014.05.009

Bretherton, F. P., and C. J. R. Garrett. 1968. Wavetrains in inhomogeneous moving media. Proc. R. Soc. Lond. Series A, *302*(1471), 529–554. https://doi.org/10.1098/rspa.1968.0034

Brown, J. M., and J. Wolf. 2009. Coupled wave and surge modelling for the eastern Irish Sea and implications for model wind-stress. Cont. Shelf Res., *29*(10), 1329–1342. https://doi.org/10.1016/j.csr.2009.03.004

Dee, D. P., S. M. Uppala, A. J. Simmons, P. Berrisford, P. Poli, S. Kobayashi, U. Andrae, et al. 2011. The ERA-interim reanalysis: Configuration and performance of the data assimilation system. Q. J. Royal Meteor Soc., *137*(656), 553–597. https://doi.org/10.1002/qj.828

Deleu, S., V. Van Lancker, D. Van den Eynde, and G. Moerkerke. 2004. Morphodynamic evolution of the kink of an offshore tidal sandbank: The Westhinder Bank (southern North Sea). Cont. Shelf Res., *24*, 1587–1610.

Dingemans, M., A. Radder, and H. D. Vriend. 1987. Computation of the driving forces of wave-induced currents. Coast. Eng., *11*(5), 539–563. https://doi.org/10.1016/0378-3839(87)90026-3

Franzetti, M., P. LeRoy, T. Garlan, D. Graindorge, A. Sukhovich, C. Delacourt, and N. Le Dantec. 2015. Long term evolution and internal architecture of a high-energy banner ridge from seismic survey of Banc du Four (western Brittany, France). Mar. Geol., *369*, 196–211. https://doi.org/10.1016/j.margeo.2015.08.019

Haas, K. A., and J. C. Warner. 2009. Comparing a quasi-3D to a full 3D nearshore circulation model: SHORECIRC and ROMS. Ocean Model., *26*(1–2), 91–103. https://doi.org/10.1016/j.ocemod.2008.09.003

Hasselmann, K. 1971. On the mass and momentum transfer between short gravity waves and larger-scale motions. J. Fluid. Mech., *50*(1), 189–205. https://doi.org/10.1017/S0022112071002520

Hasselmann, K., T. Barnett, E. Bouws, H. Carlson, D. Cartwright, K. Enke, J. Ewing, et al. 1973. Measurements of wind-wave growth and swell decay during the Joint North Sea Wave Project (JONSWAP). Deut. Hydrogr. Z. R. A., *8*, 1–95.

Huthnance, J., R. Weisse, T. Wahl, H. Thomas, J. Pietrzak, A. Souza, S. Heteren, et al. 2016. Recent change–North Sea in North Seas Region Climate Change Assessment. Cham: Springer, 85–136. https://doi.org/10.1007/978-3-319-39745-0_3

Komijani H. and Monbaliu J., 2018. The COHERENS-SWAN coupled set for wave-current interaction study in the coastal area – code modifications. Internal Report. Hydraulics laboratory (KU Leuven), Leuven, Belgium. Marine Data Archive. https://doi.org/10.14284/325

Longuet-Higgins, M. S., and R. W. Stewart. 1962. Radiation stress and mass transport in gravity waves, with application to 'surf beats'. J. Fluid. Mech., *13*(4), 481–504. https://doi.org/10.1017/S0022112062000877

Longuet-Higgins, M. S., and R. W. Stewart. 1964. Radiation stresses in water waves: A physical discussion, with applications. Deep-Sea Res. and Oceanogr. Abstr., *11*(4), 529–562. https://doi.org/10.1016/0011-7471(64)90001-4

Luyten, P. J. 1999. COHERENS: Dissemination and exploitation of a coupled hydrodynamical-ecological model for regional and shelf seas, MAS3-CT97-0088, final internal report. Management Unit of the Mathematical Models.

Luyten, P. J., I. Andreu-Burillo, A. Norro, S. Ponsar, and R. Proctor. 2005. A new version of the European public domain code COHERENS in *Proceedings* of the Fourth International Conference on EuroGOOS, Luxembourg: Office for Publications of the European Communities, 474–481.

Luyten, P. J., J. E. Jones, R. Proctor, A. Tabor, P. Tett, and K. Wild-Allen. 1999. COHERENS: A Coupled Hydrodynamical-Ecological Model for Regional and Shelf Seas, User Documentation. Belgium: Management Unit of the Mathematical Models of the North Sea.

Marsaleix, P., F. Auclair, and C. Estournel. 2009. Low-order pressure gradient schemes in sigma coordinate models: The seamount test revisited. Ocean Model., *30*(2-3), 169–177. https://doi.org/10.1016/j.ocemod.2009.06.011

Marsaleix, P., F. Auclair, J. W. Floor, M. J. Herrmann, C. Estournel, I. Pairaud, and C. Ulses. 2008. Energy conservation issues in sigma-coordinate free-surface ocean models. Ocean Model., *20*(1), 61–89. https://doi.org/10.1016/j.ocemod.2007.07.005

McWilliams, J. C., J. M. Restrepo, and E. M. Lane. 2004. An asymptotic theory for the interaction of waves and currents in coastal waters. J. Fluid Mech., *511*, 135–178. https://doi.org/10.1017/S0022112004009358

Mellor, G. 2003. The three-dimensional current and surface wave equations. J. Phys. Oceanogr., *33*(9), 1978–1989. https://doi.org/10.1175/1520-0485(2003)033<1978:TTCASW>2.0.CO;2

Mellor, G. 2005. Some consequences of the three-dimensional current and surface wave equations. J. Phys. Oceanogr., *35*(11), 2291–2298. https://doi.org/10.1175/JPO2794.1

Michaud, H., P. Marsaleix, Y. Leredde, C. Estournel, F. Bourrin, F. Lyard, C. Mayet, and F. Ardhuin. 2012. Three-dimensional modelling of wave-induced current from the surf zone to the inner shelf. Ocean Sci., *8*(4), 657–681. https://doi.org/10.5194/os-8-657-2012

Özkan-Haller, H. T., and Y. Li. 2003. Effects of wave-current interaction on shear instabilities of longshore currents. J. Geophys. Res. Oceans, *108*(C5), 1–9. https://doi.org/10.1029/2001JC001287

Ris, R., L. Holthuijsen, and N. Booij. 1994. A spectral model for waves in the near shore zone. Coast Eng. https://doi.org/10.1061/9780784400890.006

Smith, J. A. 2006. Wave-current interactions in finite depth. J. Phys. Oceanogr., *36*(7), 1403–1419. https://doi.org/10.1175/JPO2911.1

Song, Y. and D. Haidvogel. 1994. A semi-implicit ocean circulation model using a generalized topography-following coordinate system. J. Comput. Phys., *115*(1), 228–244. https://doi.org/10.1006/jcph.1994.1189

Svendsen, I. A., K. A. Haas, and Q. Zhao. 2002. Quasi-3D Nearshore Circulation Model SHORECIRC. Newark: Center for Applied Coastal Research, University of Delaware.

Svendsen, I. B., and U. Putrevu. 1990. Nearshore circulation with 3-d profiles. *in* Coastal Engineering 1990 Proceedings. B. L. Edge, ed. 22nd International Conference on Coastal Engineering, Delft, 2–6 July 1990. Charleston, SC: American Society of Civil Engineering, 241–254.

SWAN team. 2020a. SWAN Scientific and Technical Documentation, SWAN Cycle III Version 41.31A, Technical Report. Delft University of Technology.

SWAN team. 2020b. SWAN User Manual, SWAN Cycle III Version 41.31A, Technical Report. Delft University of Technology.

Thornton, E. B., and R. T. Guza. 1983. Transformation of wave height distribution. J. Geophys. Res. Oceans, *88*(C10), 5925–5938. https://doi.org/10.1029/JC088iC10p05925

Toffoli, A., L. Cavaleri, A. V. Babanin, M. Benoit, E. M. Bitner-Gregersen, J. Monbaliu, M. Onorato, A. R. Osborne, and C. T. Stansberg. 2011. Occurrence of extreme waves in three-dimensional mechanically generated wave fields propagating over an oblique current. Nat. Hazard Earth Sys. sci., *11*(3), 895–903. https://doi.org/10.5194/nhess-11-895-2011

Toffoli, A., T. Waseda, H. Houtani, L. Cavaleri, D. Greaves, and M. Onorato. 2015. Rogue waves in opposing currents: An experimental study on deterministic and stochastic wave trains. J. Fluid. Mech., *769*, 277–297. https://doi.org/10.1017/jfm.2015.132

Uchiyama, Y., J. C. McWilliams, and J. M. Restrepo. 2009. Wave-current interaction in nearshore shear instability analyzed with a vortex force formalism. J. Geophys. Res. Oceans, *114*(C6). https://doi.org/10.1029/2008JC005135

Uchiyama, Y., J. C. McWilliams, and A. F. Shchepetkin. 2010. Wave-current interaction in an oceanic circulation model with a vortex-force formalism: Application to the surf zone. Ocean Model., *34*(1–2), 16–35. https://doi.org/10.1016/j.ocemod.2010.04.002

Warner, J. C., C. R. Sherwood, R. P. Signell, C. K. Harris, and H. G. Arango. 2008. Development of a three-dimensional, regional, coupled wave, current, and sediment-transport model. Comput. Geosci., *34*(10), 1284–1306. https://doi.org/10.1016/j.cageo.2008.02.012

Waseda, T., T. Kinoshita, L. Cavaleri, and A. Toffoli. 2015. Third-order resonant wave inter-actions under the influence of background current fields. J. Fluid. Mech., *784*(), 51–73. https://doi.org/10.1017/jfm.2015.578

Yan, L. 1987. An Improved Wind Input Source Term for Third Generation Ocean Wave Modelling, scientific report. De Bilt, Netherlands: Royal Dutch Meteorolgy Institute.